Electronic Supplementary Material (ESI) for Journal of Materials Chemistry C.

Supporting Information

Multi-resonant TADF in optical cavities: Supressing excimer emission through efficient energy transfer to the lower polariton states

Inseong Cho,[a] William J. Kendrick,[b] Alexandra N. Stuart,[a] Pria Ramkissoon,[b] Kenneth P. Ghiggino,[b] Wallace W. H. Wong,[b] and Girish Lakhwani*[,a,c]

[a]*ARC Centre of Excellence in Exciton Science, School of Chemistry, The University of Sydney, NSW 2006, Australia*

[b]*ARC Centre of Excellence in Exciton Science, School of Chemistry, The University of Melbourne, Parkville, VIC 3010, Australia*

[c]*The University of Sydney Nano Institute, Sydney NSW 2006, Australia*

Corresponding author's email address: girish.lakhwani@sydney.edu.au

Contents

Additional photophysical spectra

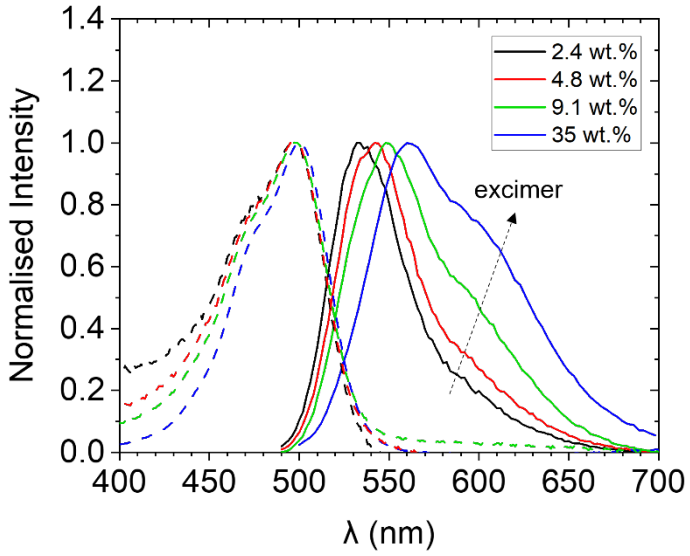

Figure S1. Absorption (dashed lines) and emission (full lines, excited at 470 nm) spectra of different concentrations of OQAO(mes)$_2$ doped in PMMA films.

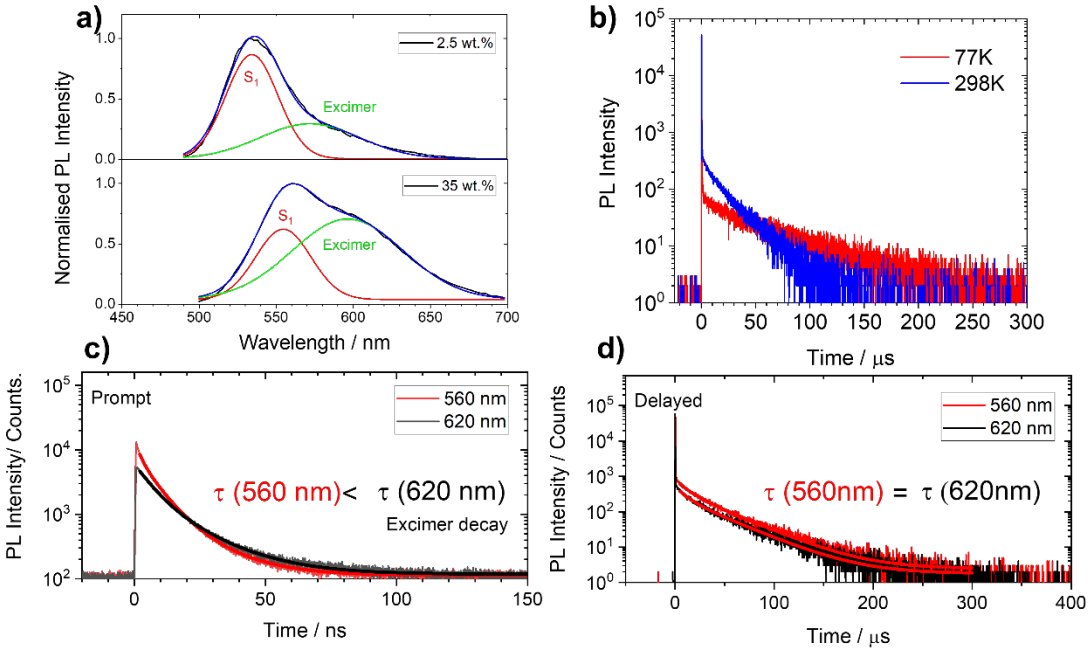

Figure S2. (a) Emission spectra of 2.4 wt% and 35 wt% OQAO(mes)$_2$ in PMMA and their deconvoluted spectra (red, green), (b) delayed emission (560 nm) of the 35 wt% OQAO(mes)$_2$ in PMMA at 77K and 298K, (c) prompt and (d) delayed emission decays of 35 wt% OQAO(mes)$_2$ in PMMA at 560 and 620 nm after excitation at 450 nm.

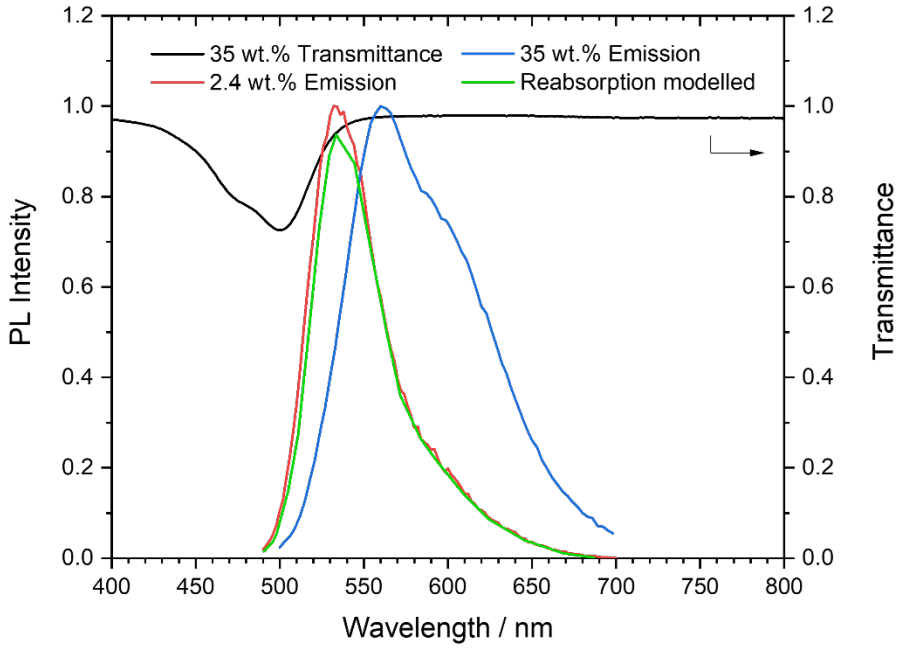

Figure S3. Emission spectra of 2.4 wt% and 35 wt% OQAO(mes)$_2$ in PMMA. Transmittance of the 35 wt% film was multiplied by the 2.4 wt% emission spectrum to model the effects of reabsorption. The shape change of the 35wt% emission cannot be accounted for by reabsorption.

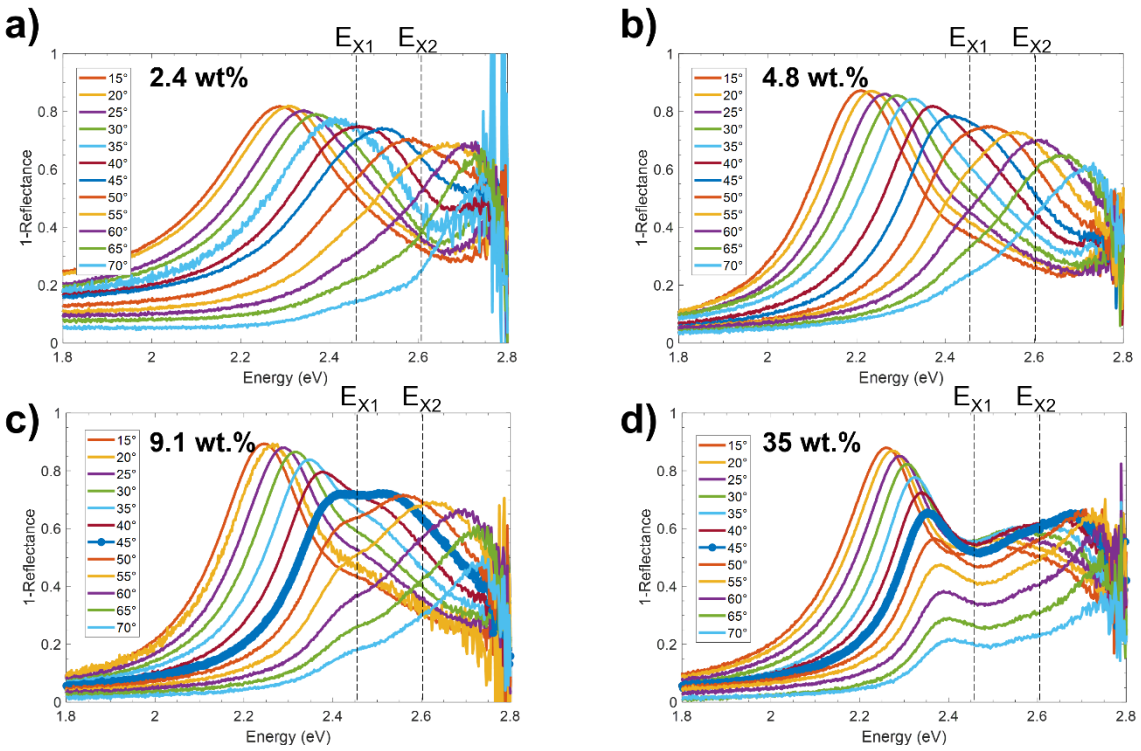

Figure S4. 1-reflectance versus energy. Reflectance was obtained using angle-resolved reflectometry on the OQAO(mes)$_2$-doped PMMA films in optical cavities at different doping concentrations. E_{X1} and E_{X2} are the exciton energies of OQAO(mes)$_2$ determined by steady-state absorption measurement.

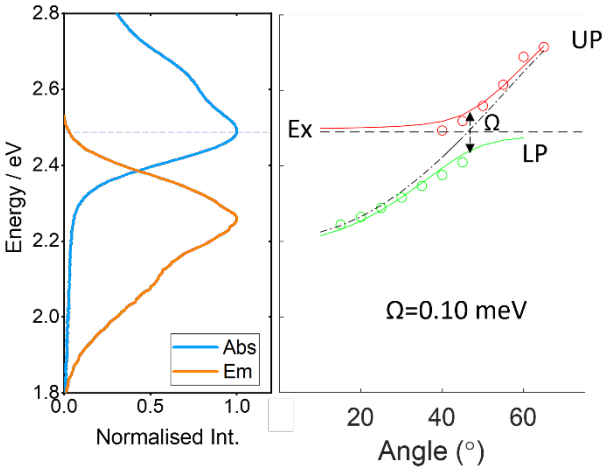

Figure S5. Absorption and emission spectra (left panel) and angular dispersion curves of 1-reflection of 9.1 wt% OQAO(mes)$_2$ in PMMA in an optical cavity. 1-reflection peaks versus angle were fit by a coupled harmonic oscillator model (Eq.S1). UP is the upper polariton, LP is the lower polariton, and Ex is the exciton energy.

Coupled harmonic oscillator model for the fitting in Figure S5.

The angular dispersion curves in **Fig. S5** were fitted to the following equation,

$$\begin{pmatrix} E_C & \Omega \\ \Omega & Ex \end{pmatrix} \begin{pmatrix} \alpha \\ \beta \end{pmatrix} = E \begin{pmatrix} \alpha \\ \beta \end{pmatrix} \qquad \text{(Eq. S1)}$$

where *Ec* is the cavity photon energy, Ω is the Rabi-splitting energy, and α and β are the Hopfield coefficients of the photon and the exciton, respectively.

Table S1. Fitting parameters for the angle-resolved reflection using harmonic oscillator models.

Parameters	9.7 wt.%	35 wt.%
N_{eff}	1.57	1.80
E_c	2.21	2.34
E_{X1}	2.49	2.45
E_{X2}	-	2.60
E_{X1} linewidth	0.22	0.13
E_{X2} linewidth	-	0.23
E_C linewidth	0.2	0.2
α^2 (LP at 45°)	0.5	0.36
β^2 (LP at 45°)	0.5	0.60
γ^2 (LP at 45°)	-	0.09

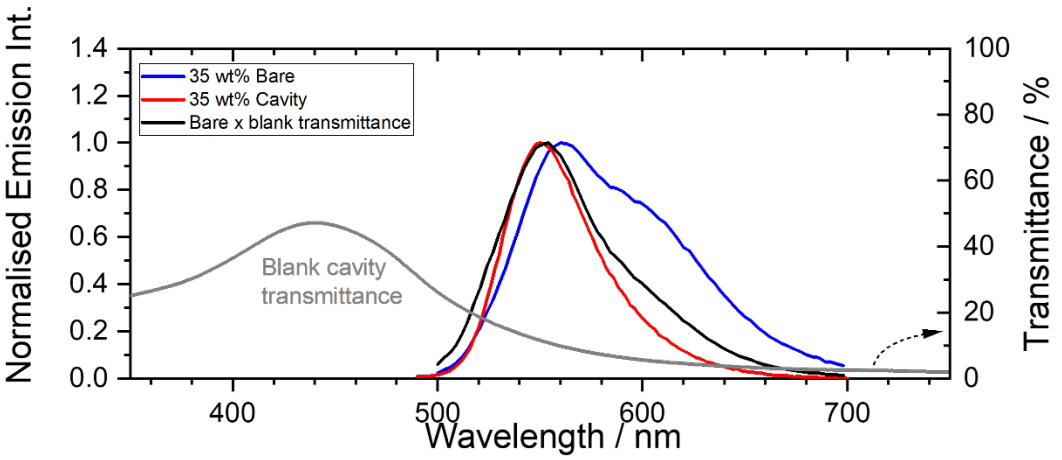

Figure S6. Emission spectra of the bare (blue), calculated (black), and measured cavity film (red), and transmittance of the blank cavity film with the same thickness.

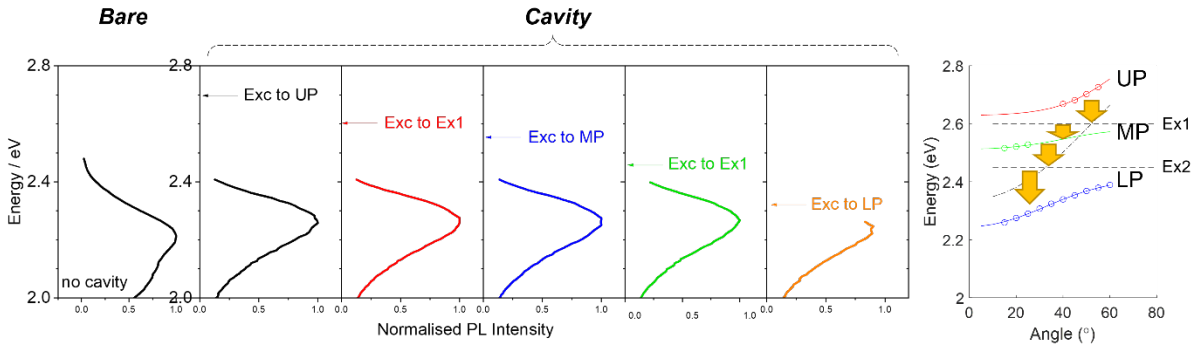

Figure S7. Emission spectra of the bare and the cavity 35 wt% OQAO(mes)$_2$ film where the cavity sample was excited (Exc) to different energy states (UP, Ex1, MP, Ex2, and LP).

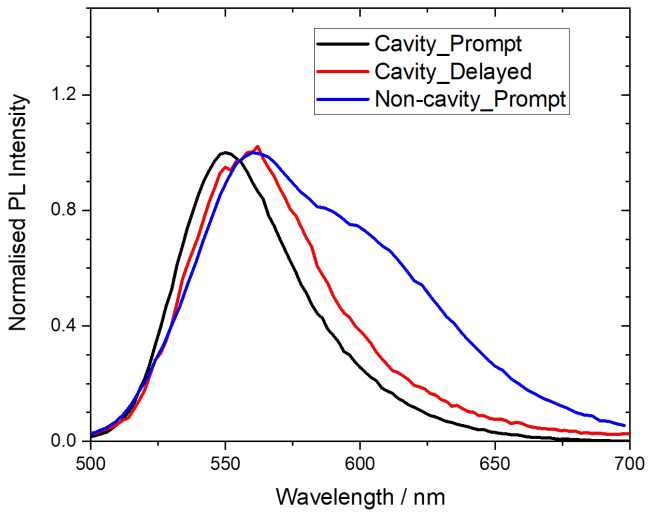

Figure S8. Steady state (prompt dominant) and delayed emission (3 µs delay) spectra (excited at 470 nm) of 35 wt% OQAO(mes)$_2$ in PMMA sandwiched between two 25 nm Ag mirrors. Blue trace is the steady-state emission of the non-cavity film.

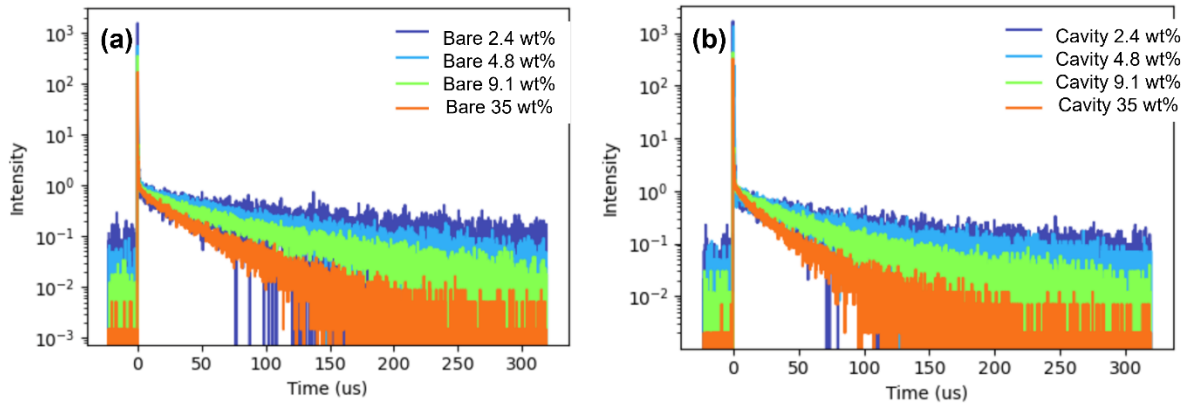

Figure S9. PL decay curves of the OQAO(mes)$_2$-doped PMMA at different concentrations (a) and those in optical cavities (b). Emission decays were measured at 540 nm for both type of film samples, except the cavity 4.8 wt% sample measured at 535 nm.

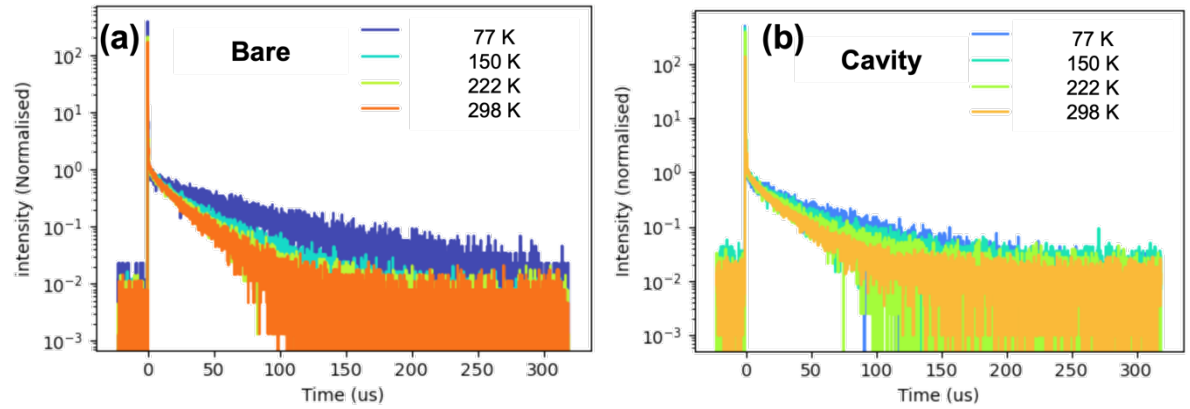

Figure S10. Temperature-dependent PL decay curves of 35 wt% OQAO(mes)$_2$ in PMMA with (a) and without (b) cavities normalised to 3 µs. Emission decays were measured at 540 nm for both type of samples.

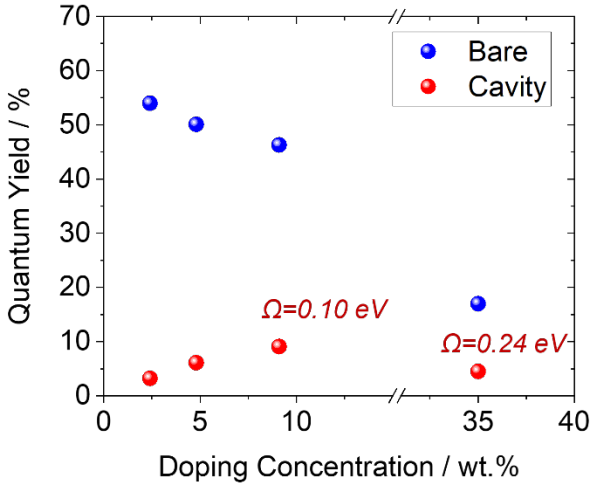

Figure 11. Photoluminescence quantum yield (PLQY) of OQAO(mes)$_2$-doped PMMA at different concentrations with and without cavities.

Kinetic modelling for the time-resolved photoluminescence (PL) decay curves.

To determine k_{RISC}, time-resolved PL decays measured using multi-channel scaling single photon counting (MCS) were fitted to a TADF model using a system of differential equations. A schematic diagram of the system with rate constants can be drawn as **Figure S12**. Here, we focus on calculating k_{RISC}, so this model does not explicitly model excimer emission.

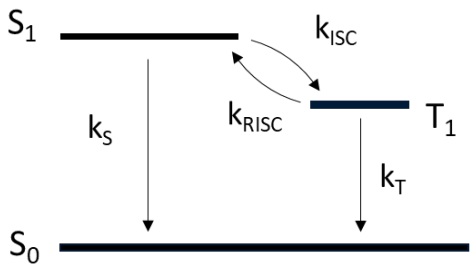

Figure S12. Schematic diagram of the exciton transition model used to fit the delayed emission.

This model can be described by the system of differential equations:

$$\frac{d[S_1]}{dt} = -k_{ISC}[S_1] - k_S[S_1] + k_{RISC}[T_1] \quad \text{(Eq. S2)}$$

$$\frac{d[T_1]}{dt} = k_{ISC}[S_1] - k_T[T_1] - k_{RISC}[T_1] \quad \text{(Eq. S3)}$$

where k_{ISC} is the rate constant of intersystem crossing, k_S is the rate constant of S_1 decay (i.e. radiative and non-radiative), k_{RISC} is the rate constant of the reverse intersystem crossing (to either S_1, excimer, or LP states), and k_T is the rate constant of the T_1 to S_0 transition (i.e. radiative and non-radiative decay). This model was convoluted with the instrument response function (approximately 100 ns) and fit to the MCS data. k_{ISC} and k_S were fixed to 2×10^8 s^{-1} and 5×10^8 s^{-1}, respectively, from the TA data (see transient absorption section). Both k_{RISC} and k_T are unknown and cannot both be fit sensitively (that is k_T can be made fast if k_{RISC} is slow to compensate, and vice versa). From the 2.4 wt% data, we determined that the maximum rate constant for k_T is 4000 s^{-1} (250 μs). Any faster than this and the model overestimates the MCS decay. Hence we fit the k_{RISC} at this upper bound for k_T, and also at the lower bound for k_T, i.e., k_T=0. The fitted rate constants are shown in Table S2, and the fits to the data shown in Figure S14. Note k_T will affect the absolute values of k_{RISC}, but not the trends with concentration, temperature, or strong-coupling. Hence in the main text we only show the case with k_T=0.

Table S2. k_{RISC} values from the fit of Equations S2 and S3 to the delayed emission data at 298 K. Rate constants were fit with k_T fixed to either 0 or 4000 s^{-1}. Error bars represent the full range of values fit to three replicate experiments.

wt%	k_T=0 (s^{-1})				k_T=4000 (s^{-1})			
	τ_{RISC} (μs)		k_{RISC} (x10^4 s^{-1})		τ_{RISC} (μs)		k_{RISC} (x10^4 s^{-1})	
	Bare	Cavity	Bare	Cavity	Bare	Cavity	Bare	Cavity
2.4	59 ± 12	53 ± 13	1.7 ± 0.3	1.9 ± 0.5	93 ± 32	77 ± 30	1.1 ± 0.4	1.3 ± 0.5
4.8	46 ± 5	41 ± 7	2.2 ± 0.2	2.4 ± 0.4	64 ± 4	45 ± 10	1.6 ± 0.1	2.2 ± 0.5
9.1	36 ± 2	28 ± 2	2.8 ± 0.2	3.6 ± 0.3	50 ± 4	36 ± 4	2.0 ± 0.2	2.8 ± 0.3
35	20 ± 1	15 ± 2	5.0 ± 0.3	6.7 ± 0.9	22 ± 2	15 ± 2	4.5 ± 0.3	6.5 ± 0.7

Table S2 shows that k_{RISC} increases with concentration, as a result of the delayed emission decay becoming faster with concentration (see Figure S9 and Figure S14). An alternative explanation for this trend could be bimolecular triplet-triplet annihilation (TTA) (Figure S13). The delayed emission data is independent of fluence, so we consider this process to be unlikely, however we investigated if this could be used to account for the changing decay rate, rather than an increasing $k_{RISC.}$ Including TTA into the model, eqn S3 becomes:

$$\frac{d[T_1]}{dt} = k_{ISC}[S_1] - k_T[T_1] - k_{RISC}[T_1] - k_{bi}[T_1][T_1] \quad \text{(Eq. S4)}$$

where k_{bi} is the rate constant of the TTA.

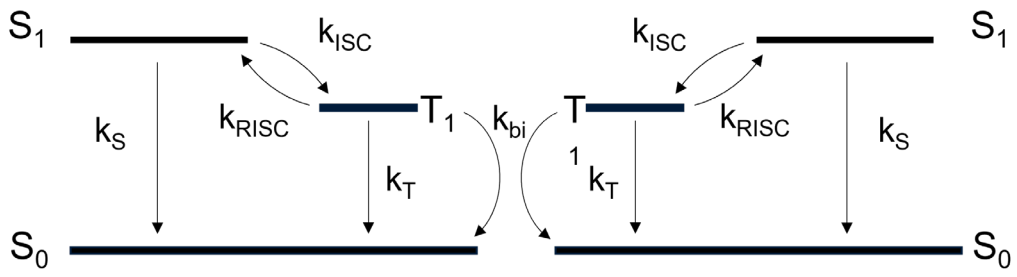

Figure S13. Schematic diagram of the exciton transition kinetic model with bimolecular process.

The TTA model was fit to the 35 wt% MCS data with k_{RISC} constrained to be the same as the 2.4 wt% (1.4×10^4 s^{-1}), and k_{bi} allowed to vary. Figure S15 shows that this model is unable to fit the data. The fit is the same for both k_T=0 or k_T=250. This demonstrates that triplet-triplet annihilation cannot explain the faster delayed fluorescence decay with concentration, and that k_{RISC} must increase, presumably due to the smaller singlet-triplet energy gap in the more aggregated state. This is consistent with the red-shift of the S_1 absorption and emission with concentration observed in the steady-state data.

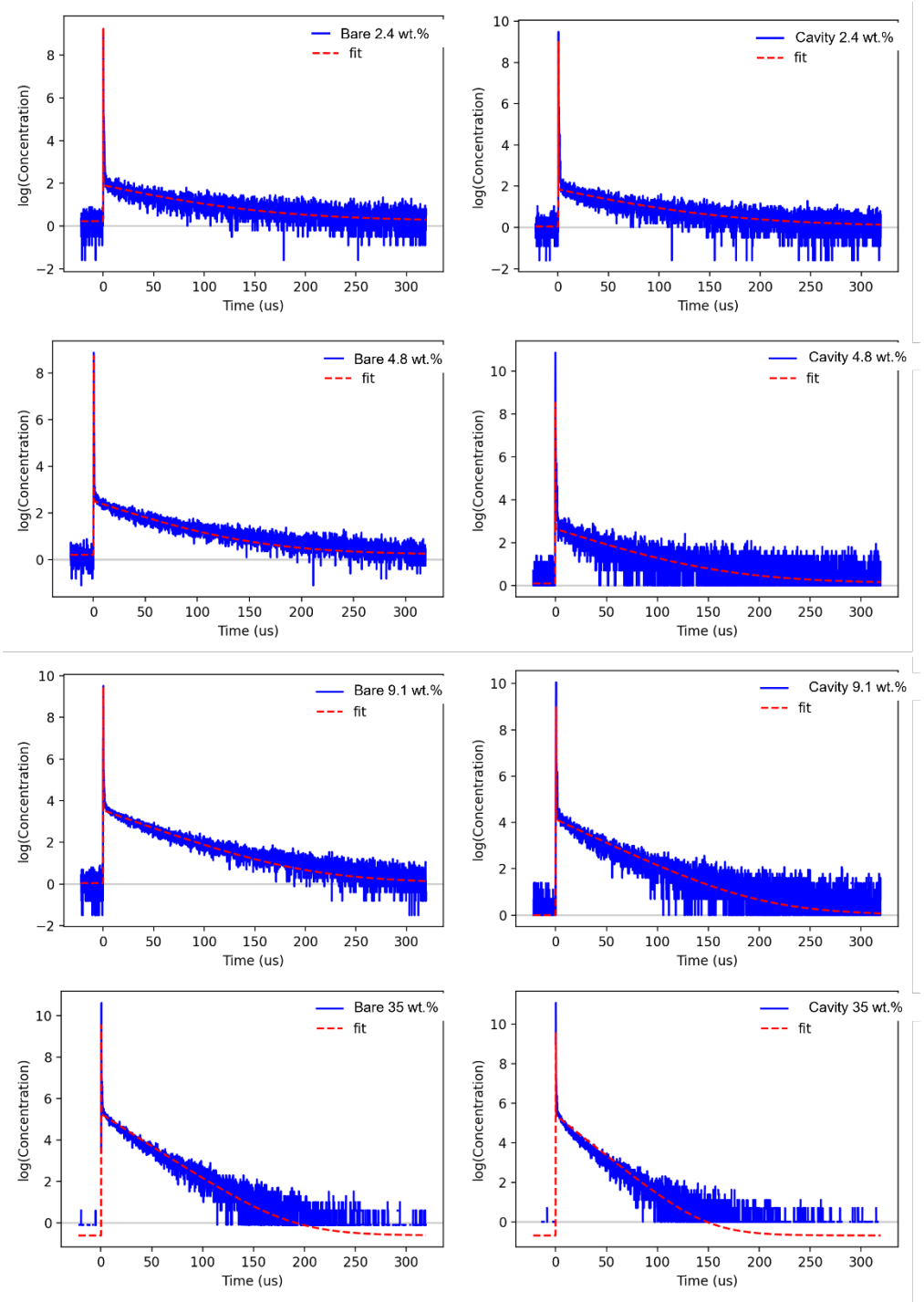

Figure S14. Delayed emission decays measured using multichannel scaling single photon counting (MCS) and fit of Equations S2 and S3 to the data.

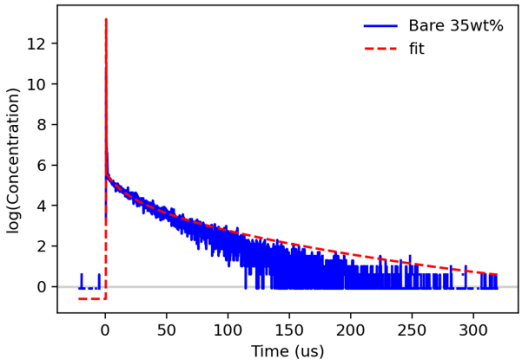

Figure S15. Delayed emission of 35 wt.% and fit of Equations S2 and S4 to the data, including triplet-triplet annihilation.

Transient Absorption Spectroscopy

Nanosecond-scale transient absorption of a 40 wt.% film was measured exciting at 355 nm and 0.6 mW. The transient absorption data is shown in Figure S16a. TCSPC shows less than 2% of the emissive species (i.e. singlet excitons and excimers) remain at 30 ns, indicating the TA spectra after this time are due to triplet excitons. To determine the rate of triplet formation, i.e. the rate of intersystem crossing k_{ISC}, the TA spectra were deconvoluted into triplet and singlet components. The singlet basis spectrum was determined from 0.5 ns, before significant triplets had formed. The triplet basis spectrum was determined from 150 ns, after the majority of singlet excitons have decayed, as shown in Figure S16b. The TA data at each delay time was fit to a linear combination of these two basis spectra:

$$\Delta A(t,\lambda) = c_{S_1}(t)\epsilon_{S_1}(\lambda) + c_{T_1}(t)\epsilon_{T_1}(\lambda) \quad \text{(Eq. S5)}$$

where $\epsilon_{S_1}(\lambda)$ and $\epsilon_{T_1}(\lambda)$ are the singlet and triplet basis spectra, and $c_{S_1}(t)$ and $c_{T_1}(t)$ are proportional to the singlet and triplet concentrations at time t. The data was able to be fit well with just two components (Figure S16c), indicating excimers are not able to resolved on this timescale or at these wavelength ranges. As such the singlet basis spectrum may contain some excimer

contributions. A more thorough analysis of the TA of OQAO is the subject of future investigations, and is beyond the scope of this work.

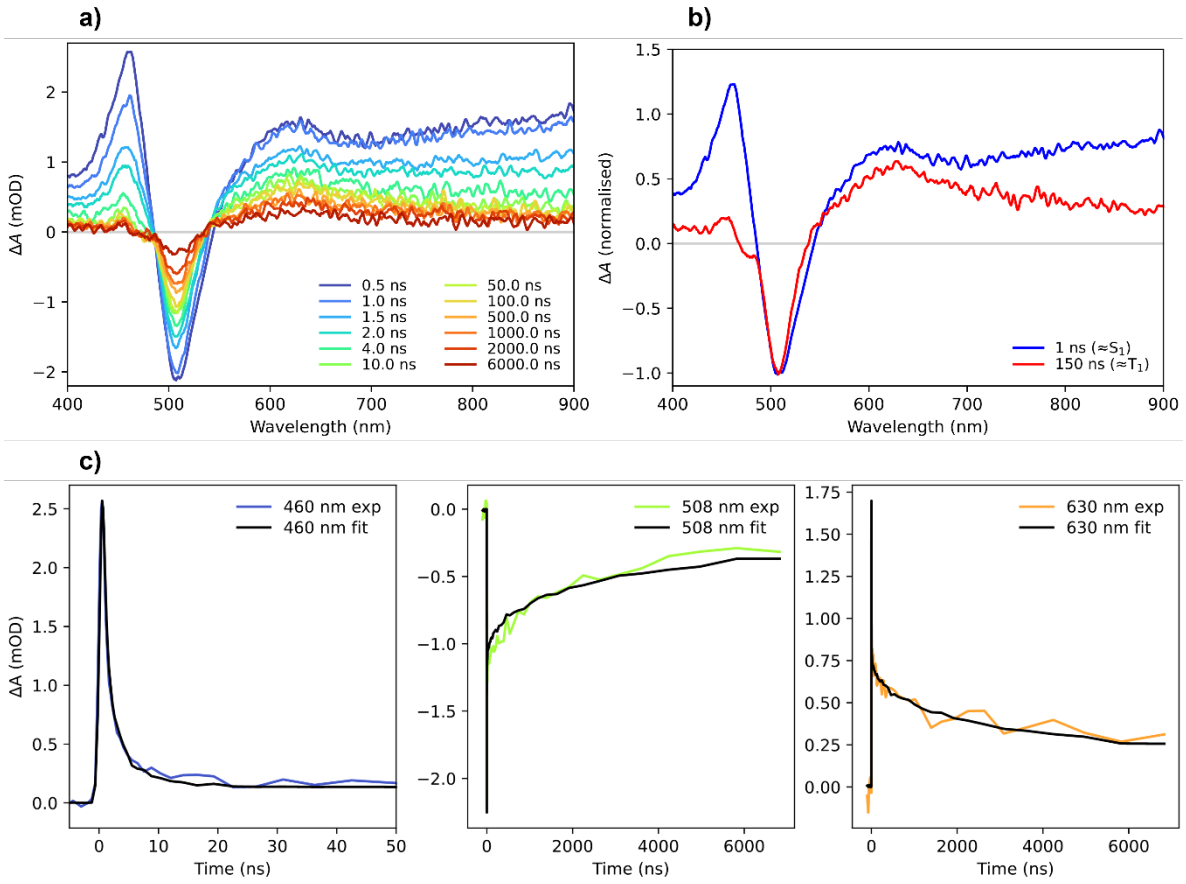

Figure S16. (a) Transient absorption spectra of 40 wt.% excited at 355 nm. (b) Basis spectra of singlet and triplet components used to deconvolute the full transient absorption spectra. (c) The fit of the TA deconvolution (i.e. sum of the S_1 and T_1 basis spectra) to the experimental data at 460 nm, 508 nm, and 630 nm.

The resulting kinetics of the singlet and triplet basis spectra ($c_{S_1}(t)$ and $c_{T_1}(t)$) are shown in Figure S17. To determine k_{ISC}, these kinetics were fit to a system of differential equations:

$$\frac{d[S_1]}{dt} = -k_{ISC}[S_1] - k_S[S_1] \quad \text{(Eq. S6)}$$

$$\frac{d[T_1]}{dt} = k_{ISC}[S_1] - k_T[T_1] \quad \text{(Eq. S7)}$$

where $[S_1]$ and $[T_1]$ are the singlet and triplet concentrations, respectively, and k_S and k_T are the intrinsic singlet and triplet lifetimes (i.e. radiative plus nonradiative decay). We ignore reverse

intersystem crossing in the TA modelling as it is not resolvable with the level of signal to noise data observed here. Similarly, we do not attempt to analyse the triplet decay kinetics due to the possibility of triplet-triplet annihilation at the relatively high fluence used for TA data. Again, a more thorough analysis of the TA kinetics, including triplet lifetimes, will be the subject of future investigations. Here we only attempt to fit the early-time data to resolve the rate of intersystem crossing. The fit of this model to the deconvoluted kinetics is shown in Figure S17. The fitted k_{ISC} is (2.4 ± 0.5) × 10^8 s^{-1} (or 4.2 ± 0.8 ns) and k_S is (5.0 ± 0.5) × 10^8 s^{-1} (or 2.0 ± 0.2 ns). k_T is fit as < 2.5 × 10^5 s^{-1} (> 4000 ns).

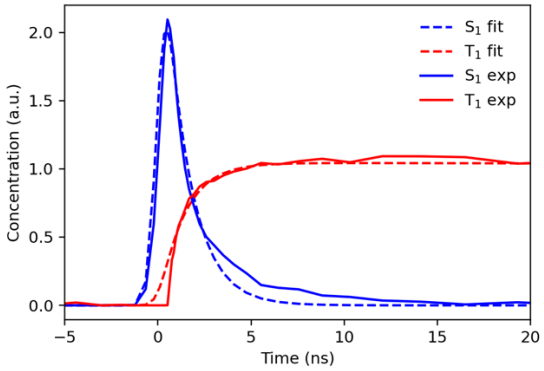

Figure S17. Deconvoluted singlet and triplet concentrations (arbitrary units) from the transient absorption data of a 40 wt% film. Also shown is the fit of Equations S6 and S7 to the deconvoluted concentrations over 20 ns.

Purcell effect

We initially fit the TADF data using the same singlet exciton decay rate (k_S) for both bare films and cavities. However, it is possible for the singlet decay rate inside the cavity to be accelerated by the Purcell effect, or the singlet lifetimes decreased by quenching the excitons at the metal interface. To determine the extent of these effects, we measured the prompt decay (TCSPC) of the 9.7 wt.% bare film and cavity (at two angles ~10 and ~45 degrees), as shown in Figure S18. Double exponential fitting results are shown in Table S3.

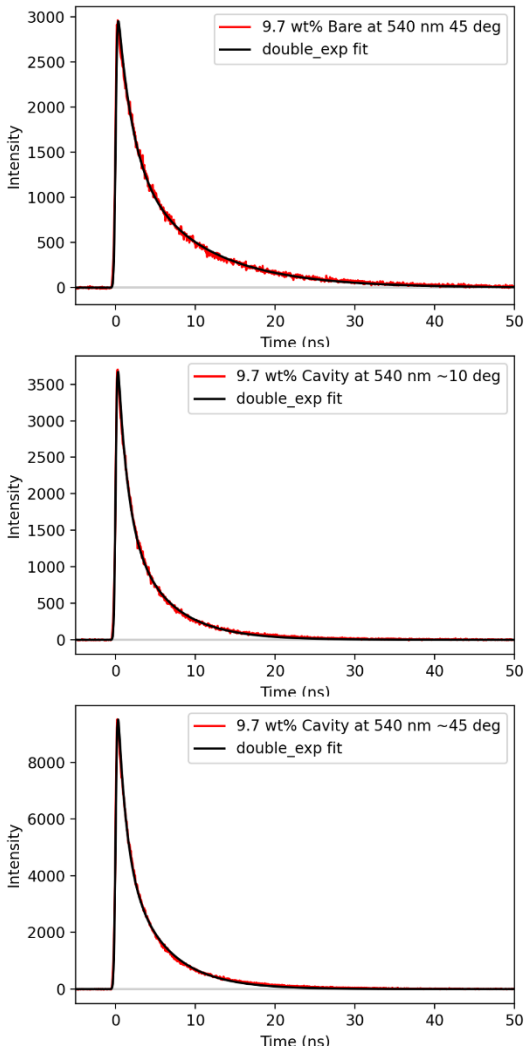

Figure S18. Prompt decay curves of 9.7 wt.% OQAO(mes)$_2$-doped PMMA (top panel) and that in the cavity. Cavity sample was measured at two angles of ~10 degrees (middle panel) and ~45 degrees (bottom panel).

Table S3. Double exponential fitting parameters of the decay curves in Figure S18.

	Bare	Cavity at 10 degrees	Cavity at 45 degrees
A_1	1895	2657	6745
τ_1	1.86 ns	1.20 ns	1.04 ns
A_2	1495	1823	5162
τ_2	9.06 ns	5.25 ns	4.98 ns

As shown in Figure S18, the prompt fluorescence lifetime is accelerated in the off-resonance cavity. The prompt decays can be fit to a biexponential with two rate constants with approximately equal weightings (the biexponential nature is potentially due to overlap with some excimer emission at this wavelength). The slower rate constant (k_2) increases by 1.73x from the bare film to the off-resonance cavity, and the faster rate constant (k_1) increases by 1.55x. This is consistent with the Purcell effect

observed by Eizner *et al.* (1.57x enhancement)[1] in other Fabry-perot cavities of similar (low) quality factor.

We thus consider 1.73x to be the upper bound of potential acceleration due to Purcell or other cavity-quenching effects, and refit the TADF model to the cavity data with $k_S \times 1.73$.

The resultant rate constants (with k_T=0) are given in Tables S4 and S5. The quality of the fits is identical to Figure S14.

Table S4. k_{RISC} values from the fit of Equations S2 and S3 to the delayed emission data at 298 K for different k_S values. Rate constants were fit with k_T fixed to 0 s^{-1}. Error bars represent the full range of values fit to three replicate experiments.

wt%	k_S=5x10^8 (s^{-1})				k_S=8.65x10^8 (s^{-1})	
	τ_{RISC} (µs)		k_{RISC} (x10^4 s^{-1})		τ_{RISC} (µs)	k_{RISC} (x10^4 s^{-1})
	Bare	Cavity	Bare	Cavity	Cavity	Cavity
2.4	59 ± 12	53 ± 13	1.7 ± 0.3	1.9 ± 0.5	66 ± 12	1.5 ± 0.3
4.8	46 ± 5	41 ± 7	2.2 ± 0.2	2.4 ± 0.4	46 ± 6	2.2 ± 0.3
9.1	36 ± 2	28 ± 2	2.8 ± 0.2	3.6 ± 0.3	32 ± 3	3.1 ± 0.3
35	20 ± 1	15 ± 2	5.0 ± 0.3	6.7 ± 0.9	17 ± 2	5.9 ± 0.7

Table S5. k_{RISC} values from the fit of Equations S2 and S3 to the delayed emission data at 35wt% for different temperatures different k_S values. Rate constants were fit with k_T fixed to 0 s^{-1}. Error bars represent the full range of values fit to three replicate experiments.

Temp	k_S=5x10^8 (s^{-1})				k_S=8.65x10^8 (s^{-1})	
	τ_{RISC} (µs)		k_{RISC} (x10^4 s^{-1})		τ_{RISC} (µs)	k_{RISC} (x10^4 s^{-1})
	Bare	Cavity	Bare	Cavity	Cavity	Cavity
77	47 ± 6	28.1 ± 0.4	2.1 ± 0.3	3.6 ± 0.1	32 ± 3	3.1 ± 0.1
150	20 ± 2	19 ± 1	5.0 ± 0.5	5.3 ± 0.3	21 ± 1	4.8 ± 0.2
222	15 ± 1	15.6 ± 0.2	6.7 ± 0.4	6.4 ± 0.1	19 ± 2	5.3 ± 0.6
298	13 ± 1	14 ± 1	7.7 ± 0.6	7.2 ± 0.5	17 ± 0.4	5.9 ± 0.1

The larger k_S value does lead to smaller k_{RISC} values, indicating that the Purcell effect (or metal interface quenching) can result in a faster delayed fluorescence decay in the cavities, as observed in the experimental data here. This is illustrated further in Figure S19, which shows the model evaluated at k_S and 1.73 × k_S, with all other rate constants kept constant.

However, the 1.73 × k_S cannot reproduce the delayed fluorescence in the cavities at all concentrations using the same RISC rate constants fit for the bare films, as shown in Tables S4 and S5. At 35 wt%,

particularly at low temperatures, the fitted k_{RISC} is still larger than that for the bare films. Figure S20 shows the 35 wt% 77 K data fit with various k_S and k_{RISC} values. When using the 35wt% bare k_{RISC} (41 µs), the fit to the data is poor, even with 1.73 × k_S. This suggests that the shorter delayed fluorescence lifetimes in the cavities cannot be entirely explained by the Purcell effect and metal quenching. Due to the low quality factors of the cavities here, the Purcell effect is small, and cannot completely account for the faster delayed fluorescence decay observed in the 35 wt.% cavity, especially at lower temperatures.

Additionally, using 1.73 × k_S at high temperatures for 35 wt% results in k_{RISC} values that are in fact smaller than the bare case (note that the temperature-dependent data has a higher resolution than the concentration-dependent data, hence the smaller errors in Table S5 compared to S4). This suggests that the 1.73 times enhancement of k_s in the cavities is likely a significant overestimate. We expect that most of the enhanced prompt decay lifetime is due to a decrease in excimer emission at the measured wavelength (540 nm), which is slower than S_1 or polariton emission. Ultimately, due to the lower quality factors of the cavities the Purcell effect is small, and cannot explain all the observed differences between the cavities and the bare films.

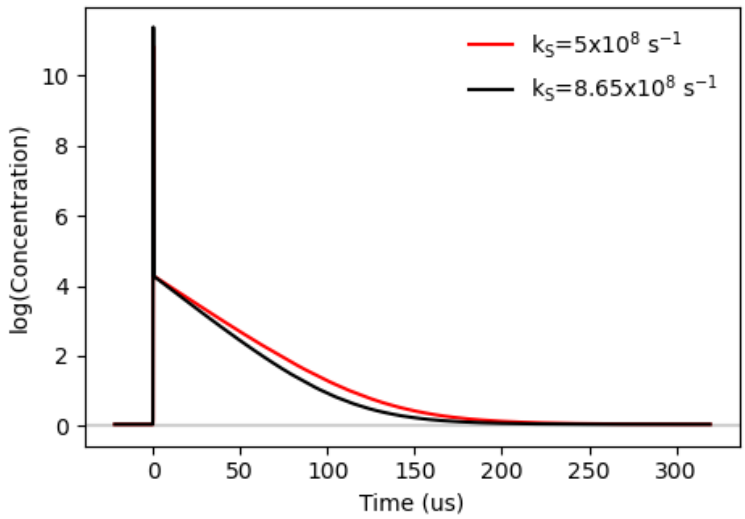

Figure S19. TADF model evaluated with k_{RISC}=5x10^4 s^{-1}, k_T=0 s^{-1}, k_{ISC}=2x10^8 s^{-1} and k_S indicated in the legend. Enhancement of k_S (e.g by the Purcell effect) can cause a small decrease in the delayed fluorescence lifetime.

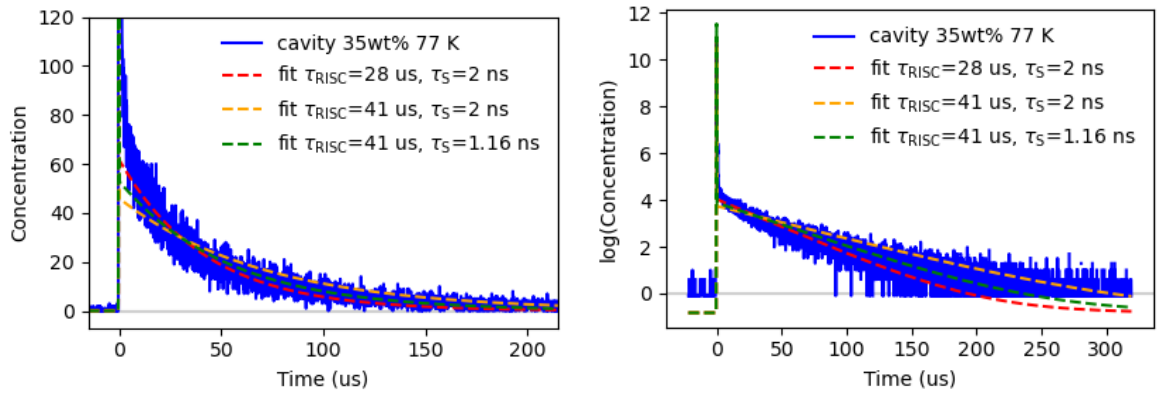

Figure S20. TADF model fit to the 35 wt%, 77 K cavity data with various k_S and k_{RISC} rate constants. The lower bound of the bare RISC rate constant (41 µs) is unable to fit the data, even when possible k_S enhancement due to the Purcell effect is considered.

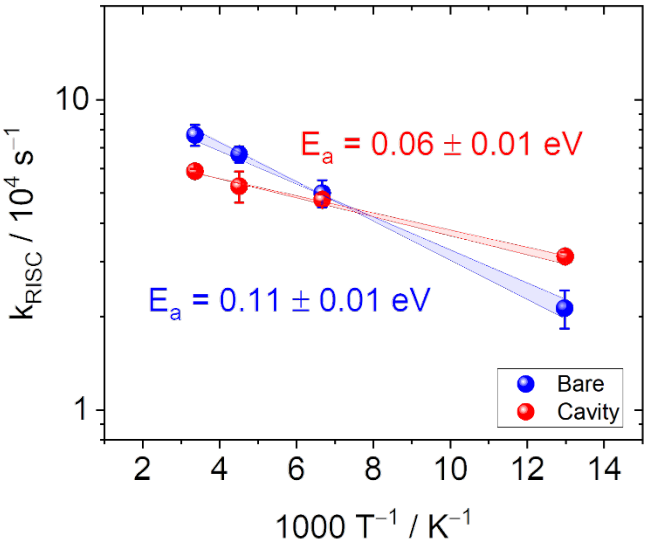

Figure S21. k_{RISC} versus 1000/T of 35 wt.% OQAO(mes)$_2$ in PMMA with and without cavity. k_{RSIC} for the cavities were modelled using k_s=8.65 × 10^8 s^{-1}.

Synthetic details

General experimental

Unless otherwise indicated, all reagents and solvents were purchased from commercial sources and used without further purification. Anhydrous dichloromethane (CH_2Cl_2) was obtained from alumina drying columns. Anhydrous methanol (MeOH) and dimethylformamide (DMF) were obtained by drying over 3 Å and 4 Å activated molecular sieves respectively. For reactions carried out under inert conditions, standard Schlenk techniques were used. Solvents were sparged with nitrogen gas for several hours prior to use and the reaction vessels were sealed with a rubber septum under a nitrogen atmosphere. Thin layer chromatography (TLC) was done using Merck-Millipore Silica gel glass plates (60G F254), with a 254 nm and 365 nm light mercury lamp used for identifying spots.

^{1}H NMR (500 or 600 MHz) and ^{13}C NMR (101, 126, 151 MHz) spectra were acquired with a 400 MHz JEOL spectrometer, a 500 MHz Agilent DD2 spectrometer, or a 600 MHz Bruker Avance III spectrometer, and chemical shifts were referenced to the residual solvent peaks. High-resolution mass spectra were acquired using a Thermo Scientific Q Exactive Plus Orbitrap LC-MS/MS instrument.

UV–Vis spectroscopy was performed on an Agilent Technologies Cary 50 UV–Vis. Photoluminescence spectroscopy was performed on a Varian Cary Eclipse fluorimeter.

Synthetic procedures

1, phenoxazine and mesitylboronic acid were purchased from commercial suppliers and used without further purification. **2** and **4** were synthesised as reported, with characterisation data matching the literature.[2,3]

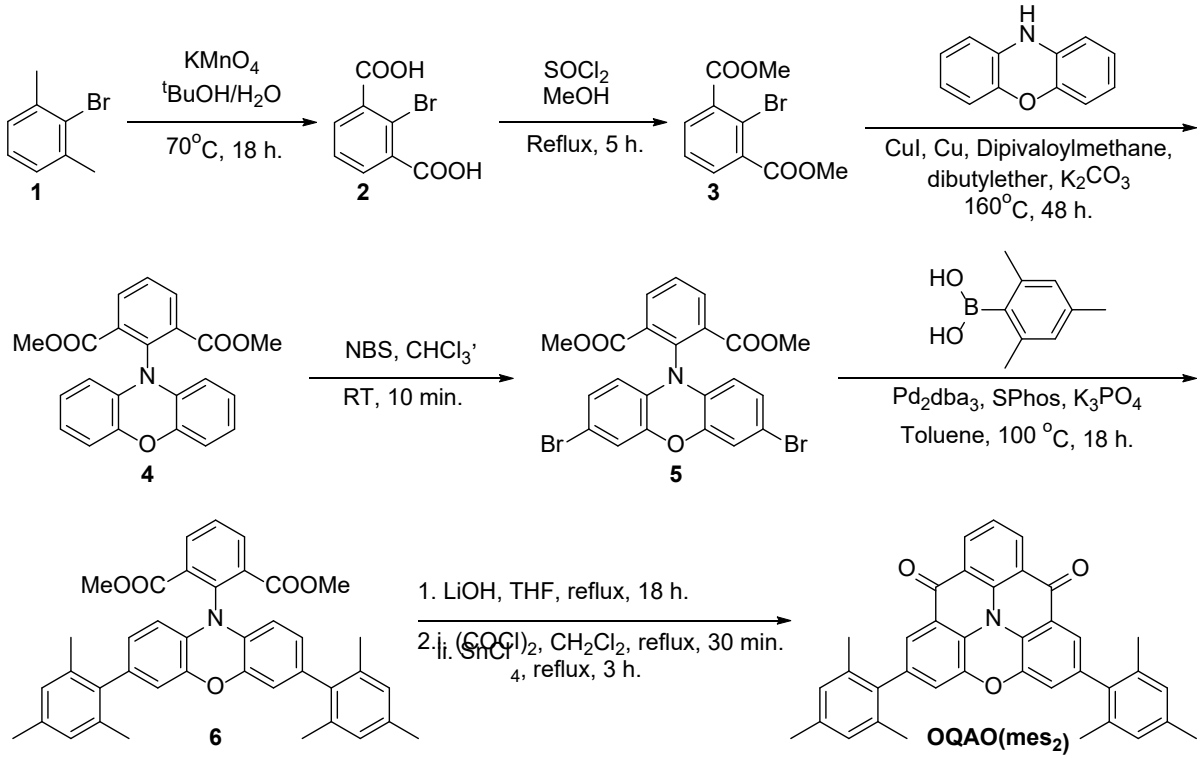

Scheme S1. Synthetic scheme for the synthesis of **OQAO(mes)²**

Dimethyl 2-bromoisophthalate (**3**)

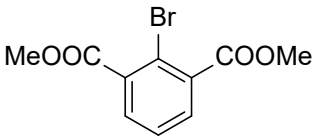

Thionyl chloride (15 mL, 207 mmol) was added dropwise to a stirred solution of dry MeOH (500 mL) at 0 ℃. 2-bromoisophthalic acid (23.0 g, 93.9 mmol) was added and the reaction mixture warmed to reflux and stirred for 5 hours. The reaction solvent was removed *in vacuo* followed by addition and consecutive removal *in vacuo* of toluene three times. The final residue was passed through a short silica plug in $CHCl_3$. Removing solvents *in vacuo* yielded **3** as a clear, slightly orange oil (23.7g, 92%).

^{1}H NMR (600 MHz, $CDCl_3$): δ (ppm) δ 7.66 (d, *J* = 7.8 Hz, 2H), 7.37 (t, *J* = 7.8 Hz, 1H), 3.90 (s, 6H).

^{13}C NMR (151 MHz, $CDCl_3$): δ (ppm) δ 166.9, 135.4, 132.3, 127.2, 119.1, 52.8.

HRMS (ESI): m/z = 272.9759 ($C_{10}H_{10}BrO_4$, $[M+H]^+$ requires 272.9757)

Dimethyl 2-(3,7-dibromo-10H-phenoxazin-10-yl)isophthalate (**5**)

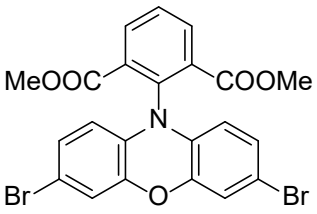

Dimethyl 2-(10H-phenoxazin-10-yl)isophthalate (**4**) (2.08 g, 5.54 mmol) was stirred in $CHCl_3$ (105 mL) at room temperature. Freshly recrystallised N-bromosuccinimide (2.02 g, 11.36 mmol) was added portionwise and the reaction monitored by thin-layer chromatography. After 10 minutes the TLC showed full conversion. The reaction mixture was passed through a short silica plug in $CHCl_3$. The solvent was removed *in-vacuo*. The resulting residue was redissolved in a minimum amount of CH_2Cl_2 and precipitated via layered addition of MeOH, affording the final product as a deep orange crystalline solid (2.30 g over two recrystallisations, 78%).

^{1}H NMR (500 MHz, $CDCl_3$): δ (ppm) δ 8.23 (d, J = 7.8 Hz, 2H), 7.67 (t, J = 7.8 Hz, 1H), 6.82 (d, J = 2.2 Hz, 2H), 6.67 (dd, J = 8.5, 2.2 Hz, 2H), 5.57 (d, J = 8.5 Hz, 2H), 3.79 (s, 6H).

^{13}C NMR (126 MHz, $CDCl_3$): δ (ppm) δ 165.3, 144.3, 136.6, 136.2, 133.9, 132.7, 129.6, 126.3, 118.8, 114.2, 113.1, 53.2.

HRMS (ESI): m/z = 533.9375 ($C_{22}H_{16}Br_2NO_5$, $[M+H]^+$ requires 533.9376)

Dimethyl 2-(3,7-dimesityl-10H-phenoxazin-10-yl)isophthalate (**6**)

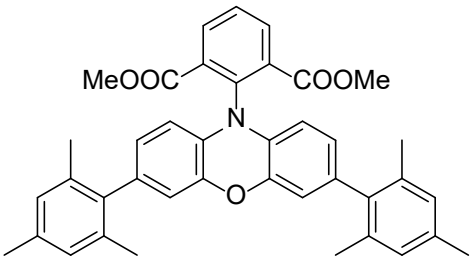

Dimethyl 2-(3,7-dibromo-10H-phenoxazin-10-yl)isophthalate (**5**) (1.25 g, 2.34 mmol), mesitylboronic acid (1.54 g, 9.38 mmol) and tribasic potassium phosphate (3 g, 14.1 mmol) were dissolved in toluene (60 mL) under N_2 atmosphere. The solution was degassed via sparging with N_2 for 30 mins. Tris(dibenzylideneacetone)dipalladium(0) (107 mg, 0.12 mmol) and SPhos (96 mg, 0.23 mmol) were added and the solution was heated to 100 ℃ for 18 hours. The reaction mixture was cooled to room temperature and filtered through a silica plug in $CHCl_3$, affording a yellow oil that crystallised over 15 minutes. The solid was redissolved in a minimum amount of CH_2Cl_2 and subsequently recrystallised from careful layered addition of methanol, affording the final product as bright yellow crystals (1.17 g, 82%).

^{1}H NMR (600 MHz, Acetone-d_6): δ (ppm) δ 8.27 (d, J = 7.8 Hz, 2H), 7.84 (t, J = 7.8 Hz, 1H), 6.88 (s, 4H), 6.46 (d, J = 1.8 Hz, 2H), 6.36 (dd, J = 8.1, 1.8 Hz, 2H), 5.90 (d, J = 8.1 Hz, 2H), 3.77 (s, 6H), 2.25 (s, 6H), 2.03 (s, 12H).

^{13}C NMR (101 MHz, Acetone-d_6): δ (ppm) 166.3, 144.6, 138.9, 138.0, 137.00, 136.6, 136.2, 135.4, 135.3, 133.2, 130.3, 128.8, 124.8, 116.9, 114.2, 53.0, 21.1, 20.8.

HRMS (ESI): m/z = 612.2752 ($C_{40}H_{38}NO_5$, $[M+H]^+$ requires 612.2745)

OQAO(mes)$_2$

To a solution of dimethyl 2-(3,7-dimesityl-10H-phenoxazin-10-yl)isophthalate (**6**) (1.15 g, 1.88 mmol) in THF (31.3 mL) was added a suspension of LiOH (900 mg, 37.6 mmol) in water (9.50 mL). The resulting mixture was refluxed for 18 hours. Upon full conversion vis ESI-MS the solution was cooled to room temperature. THF was removed *in-vacuo* and the resulting crude reaction mixture diluted with water (30 mL), acidified to pH 5-6 and extracted thrice with Et_2O. Drying of the organic layer followed by removal of solvents *in-vacuo* afforded the diacid as pale yellow solid (1 g) which was taken immediately to the next step.

HRMS (ESI): m/z = 582.2275 ($C_{38}H_{32}NO_5$, $[M-H]^-$ requires 582.2286)

The diacid (1 g, 1.71 mmol) was dispersed in dry CH_2Cl_2 in an oven dried microwave vial under an N_2 atmosphere. Two drops of anhydrous DMF were added followed by dropwise addition of oxalyl chloride (323 µL, 3.77 mmol). The reaction was heated to 45 °C for 30 minutes. After cooling to room temperature, $SnCl_4$ (441 µL, 3.77 mmol) was added dropwise to the reaction mixture. The reaction mixture was heated to 45 °C for 3 hours. The reaction mixture was added dropwise to 1 M NaOH followed by extraction of the aqueous phase with CH_2Cl_2, drying of the organic phase over $MgSO_4$ and removal of solvents *in-vacuo*. The resulting solid was recrystallised by layered addition of MeOH to a solution of the product in CH_2Cl_2 to give **OQAO(mes)$_2$** as a red powder (530 mg, 51% over two steps).

^{1}H NMR (600 MHz, $CDCl_3$): δ (ppm) δ 8.96 (d, *J* = 7.7 Hz, 2H), 7.88 (d, *J* = 1.9 Hz, 2H), 7.73 (t, *J* = 7.7 Hz, 1H), 7.12 (d, *J* = 1.9 Hz, 2H), 6.98 (s, 4H), 2.35 (s, 6H), 2.09 (s, 12H).

^{13}C NMR (101 MHz, $CDCl_3$): δ (ppm) 176.47, 143.97, 139.92, 137.66, 136.56, 135.86, 134.94, 134.53, 128.51, 125.74, 123.97, 123.43, 122.37, 122.17, 121.26, 21.20, 20.83.

HRMS (ESI): m/z = 548.2226 ($C_{38}H_{30}NO_3$, $[M+H]^+$ requires 548.2220)

UV-vis ($CHCl_3$): λ_{max}/nm ($\varepsilon/10^3$ M^{-1} cm^{-1}) = 503 (16.2), 481 (11.9), 320 (11.4)

Fluorescence ($CHCl_3$): λ_{max}/nm = 535

Characterization data

Dimethyl 2-bromoisophthalate (3)

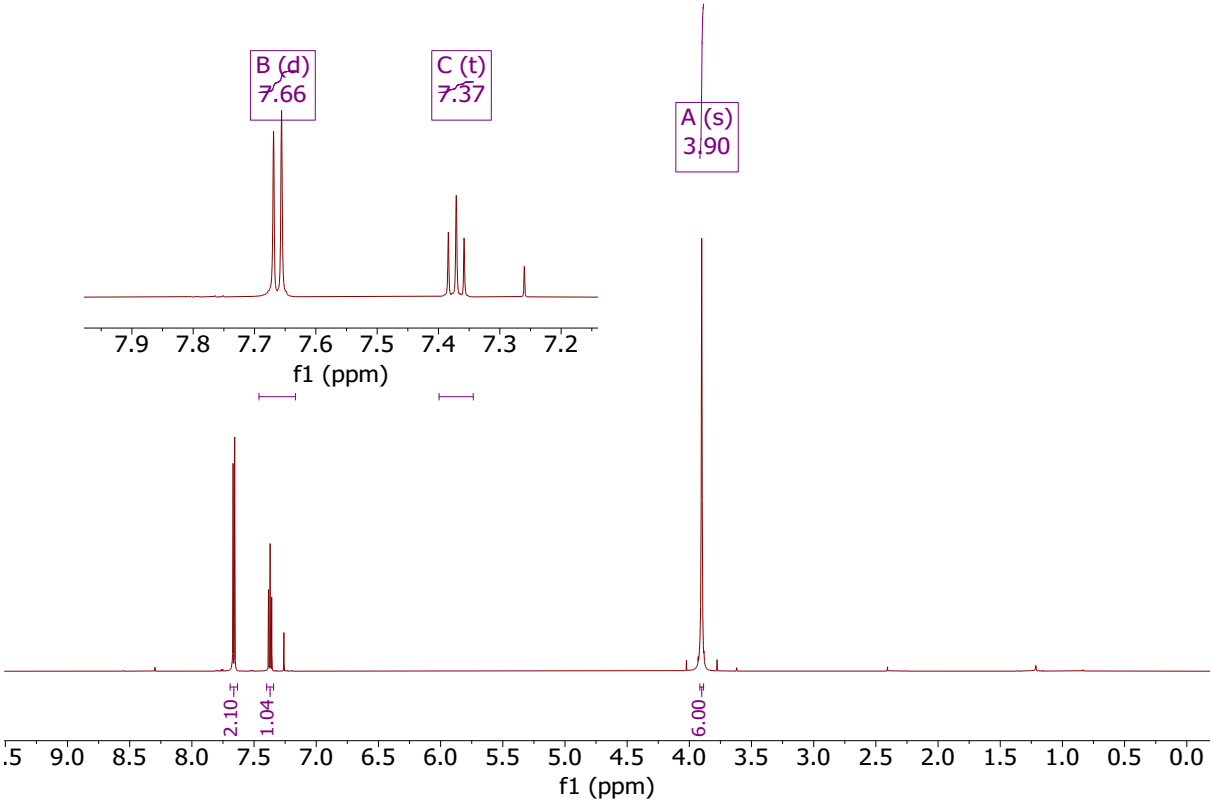

Figure S22. ^{1}**H NMR** (600 MHz, $CDCl_3$) spectrum of **3**.

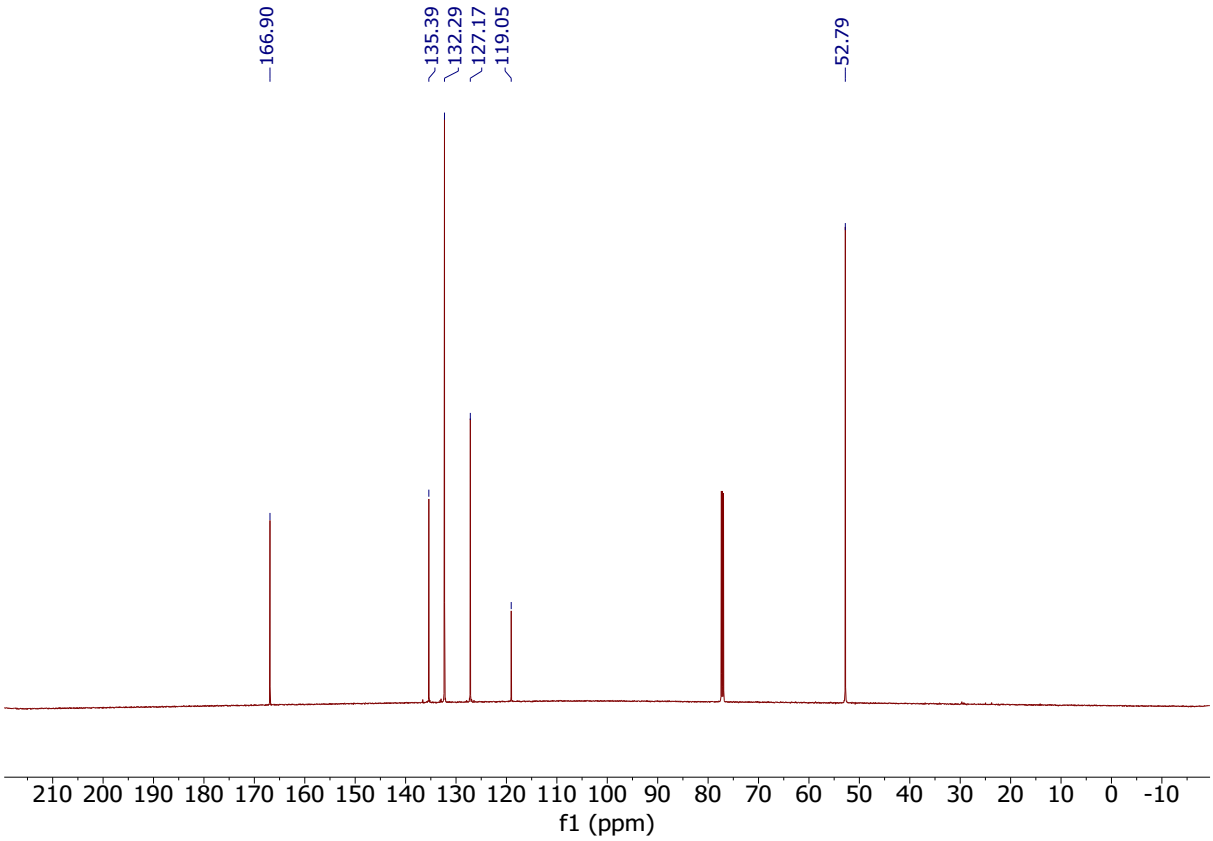

Figure S23. ^{13}**C NMR** (151 MHz, CDCl3) of **3**.

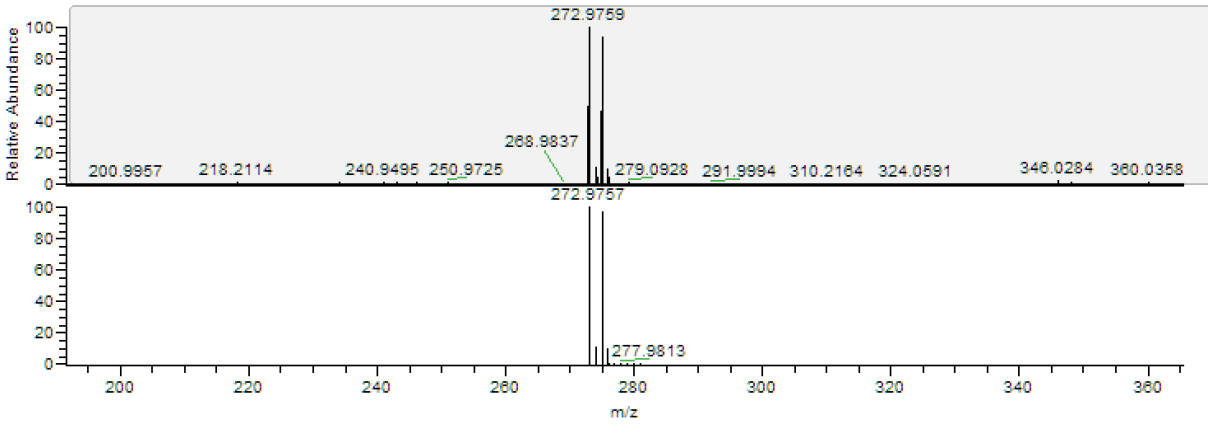

Figure S24. ESI-MS (positive ionisation) spectrum of **3** (top) and predicted isotopic profile (bottom).

Dimethyl 2-(3,7-dibromo-10H-phenoxazin-10-yl)isophthalate (**5**)

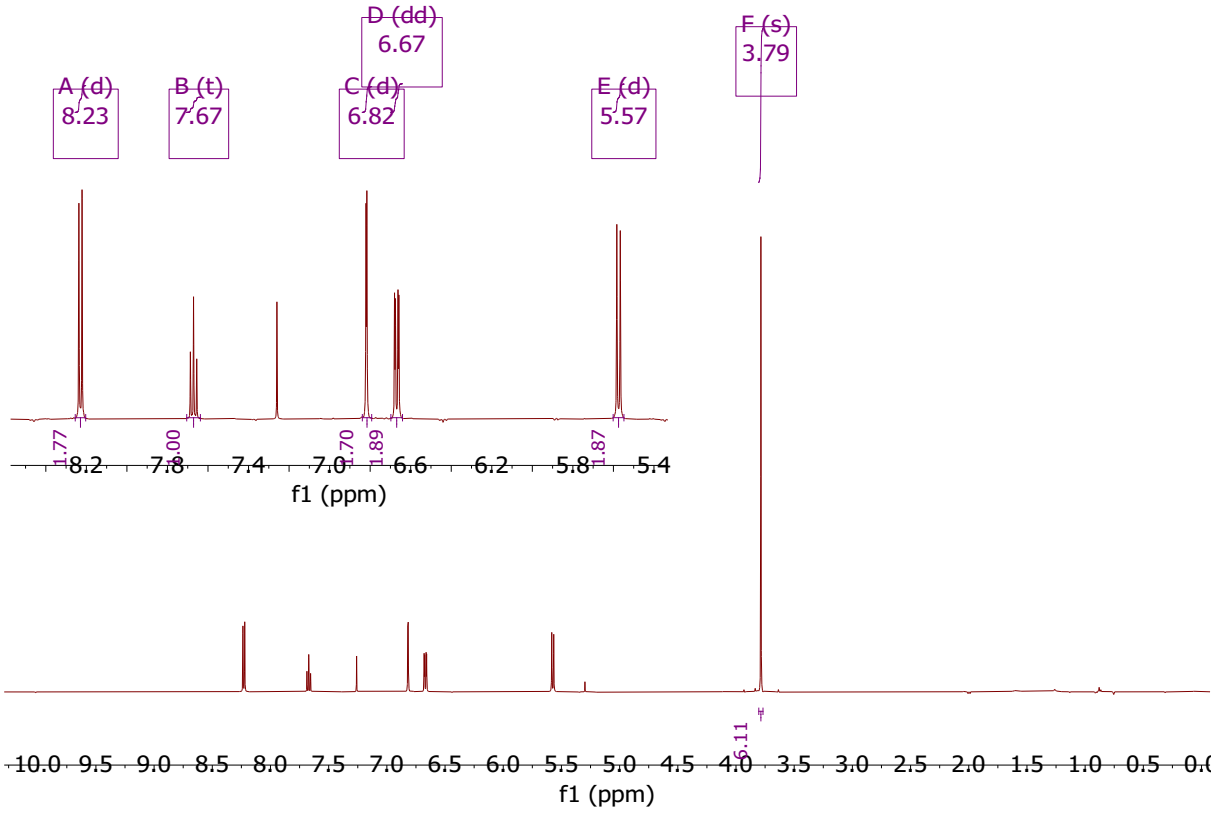

Figure S25. ^{1}**H NMR** (500 MHz, $CDCl_3$) of **5**.

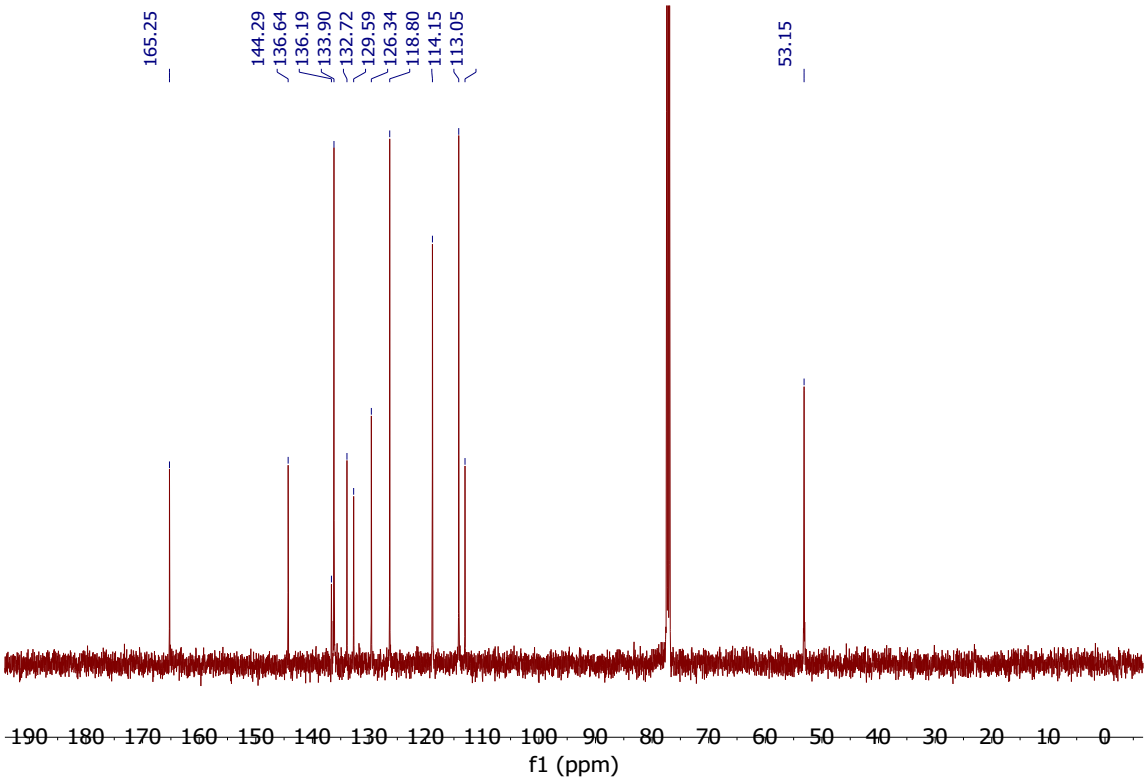

Figure S26. ^{13}**C NMR** (126 MHz, $CDCl_3$) of **5**.

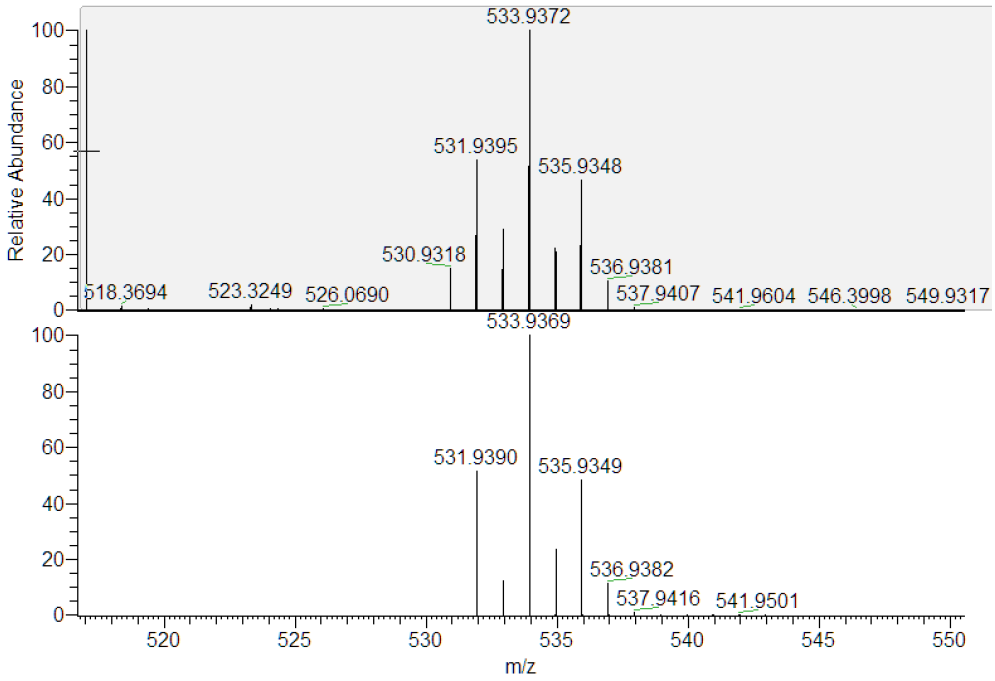

Figure S27. ESI-MS (positive ionisation) spectrum of **5** (top) and predicted isotopic profile (bottom).

Dimethyl 2-(3,7-dimesityl-10H-phenoxazin-10-yl)isophthalate (6)

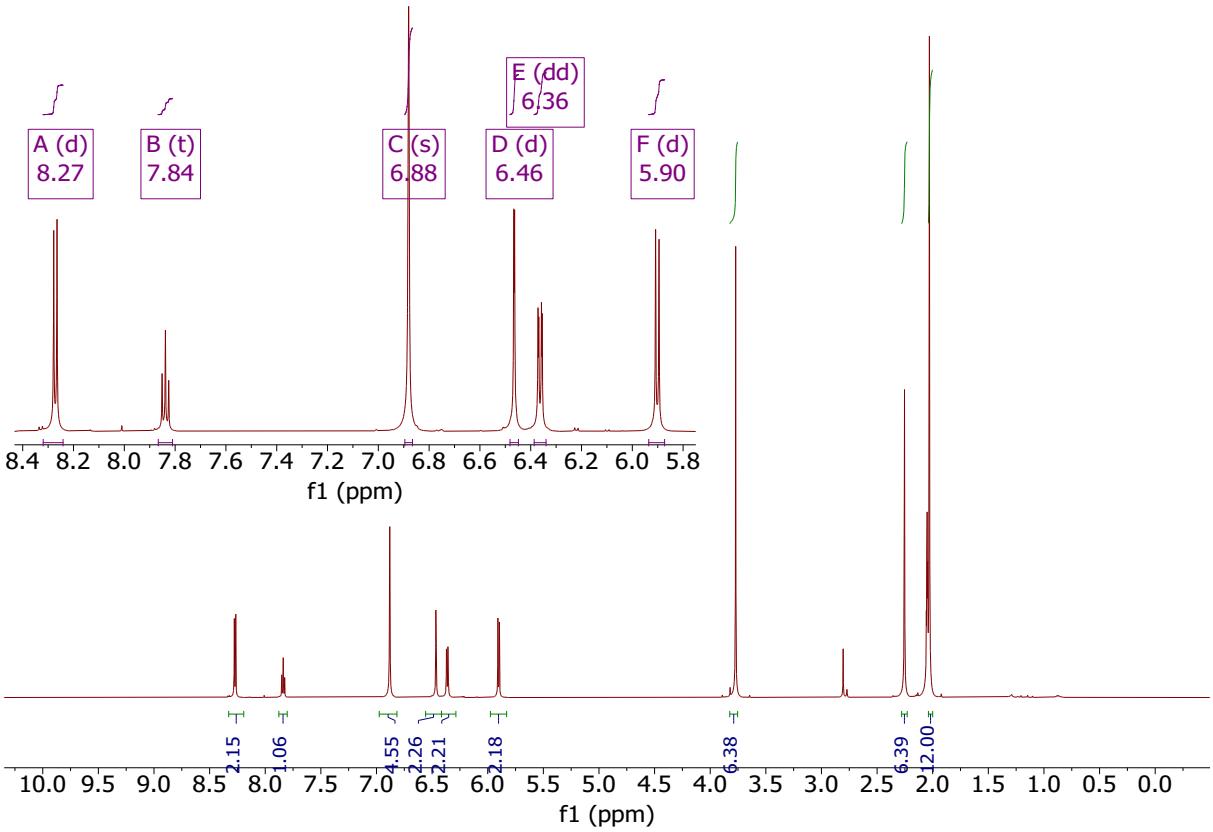

Figure S28. ^{1}**H NMR** (600 MHz, Acetone-d_6) of **6**.

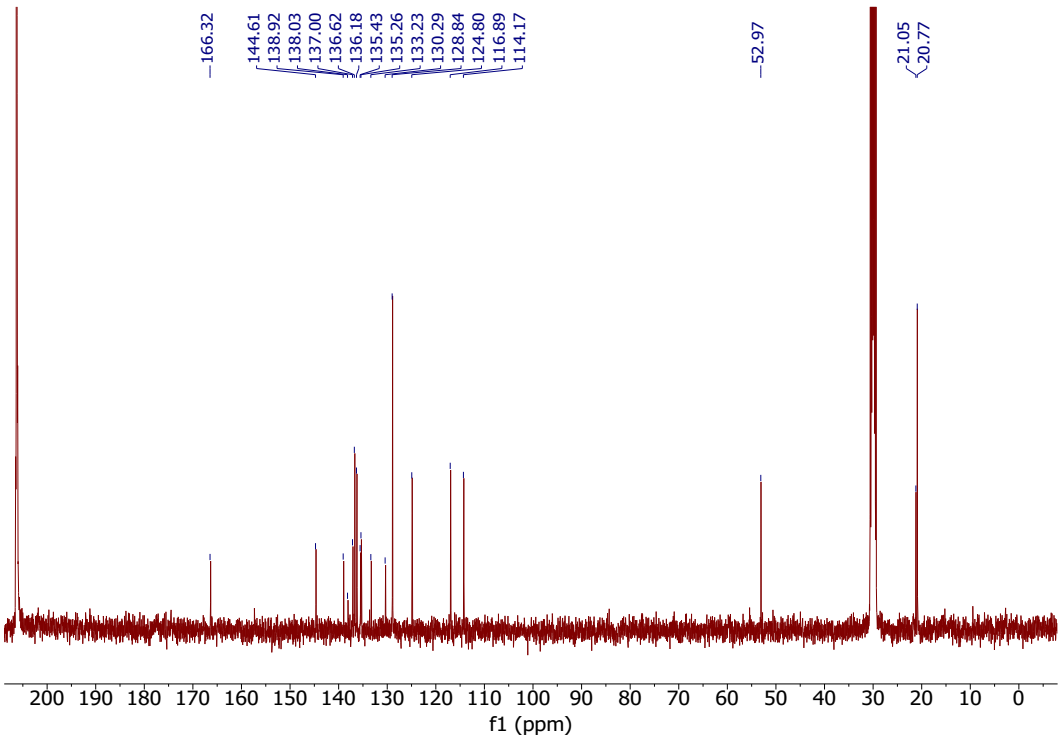

Figure S29. ^{13}**C NMR** (101 MHz, Acetone-d_6) of **6**.

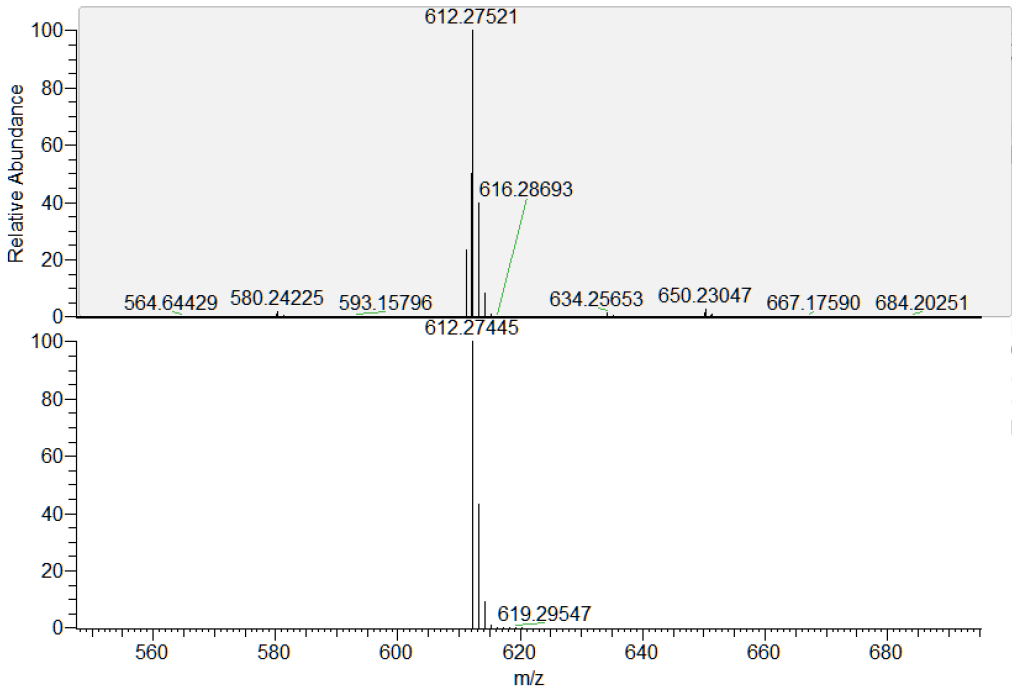

Figure S30. ESI-MS (positive ionisation) spectrum of **6** (top) and predicted isotopic profile (bottom).

OQAO(mes)$_2$

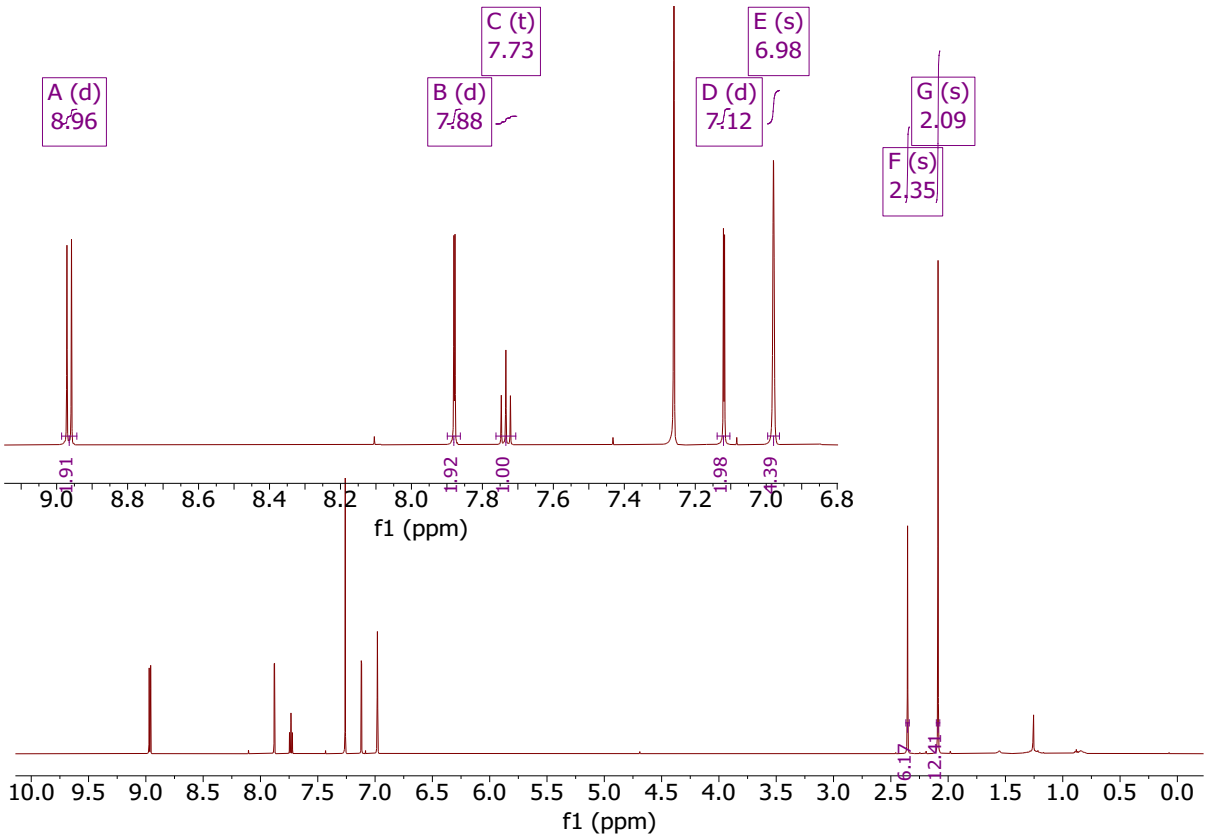

Figure S31. ^{1}H NMR (600 MHz, $CDCl_3$) of **OQAO(mes)$_2$**.

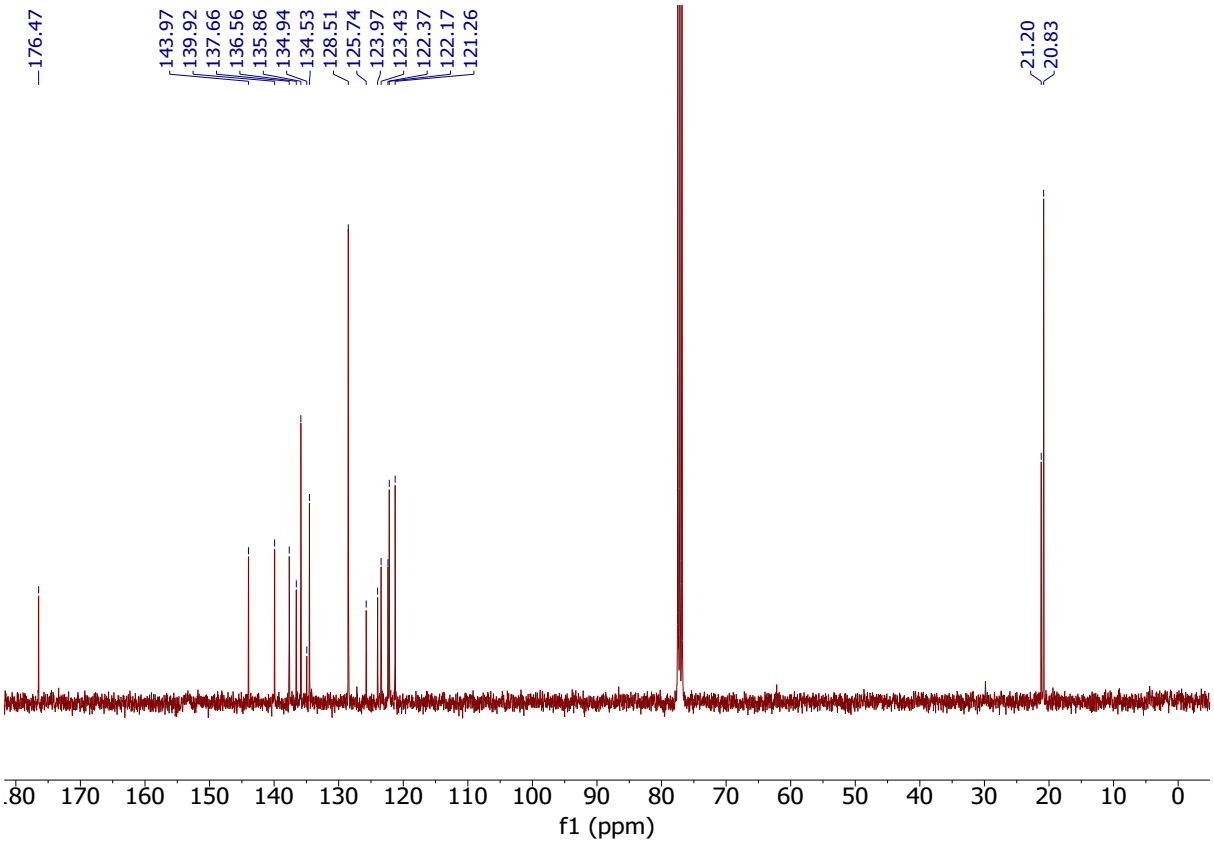

Figure S32. ^{13}**C NMR** (101 MHz, $CDCl_3$) of **OQAO(mes)$_2$**.

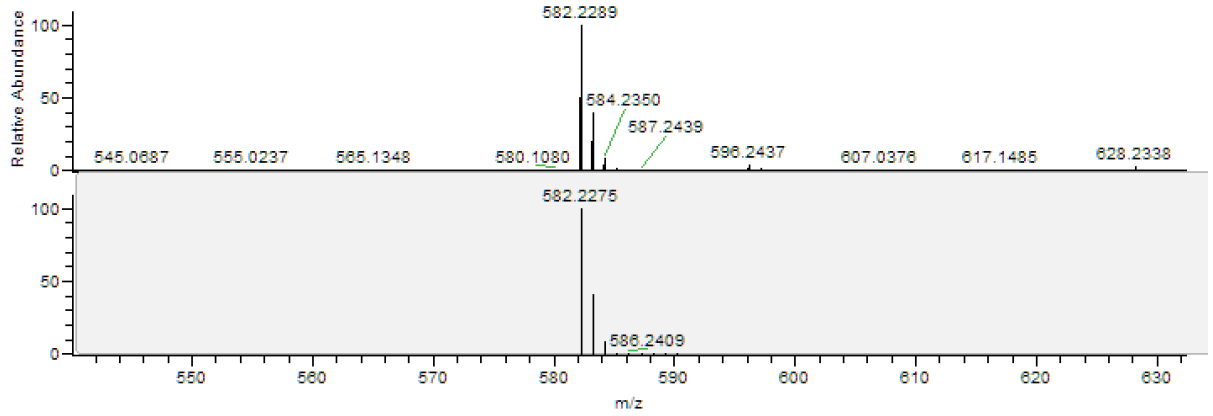

Figure S33. ESI-MS (negative ionisation) spectrum of the diacid intermediate in the synthesis of **OQAO(mes)$_2$** (top) and predicted isotopic profile (bottom).

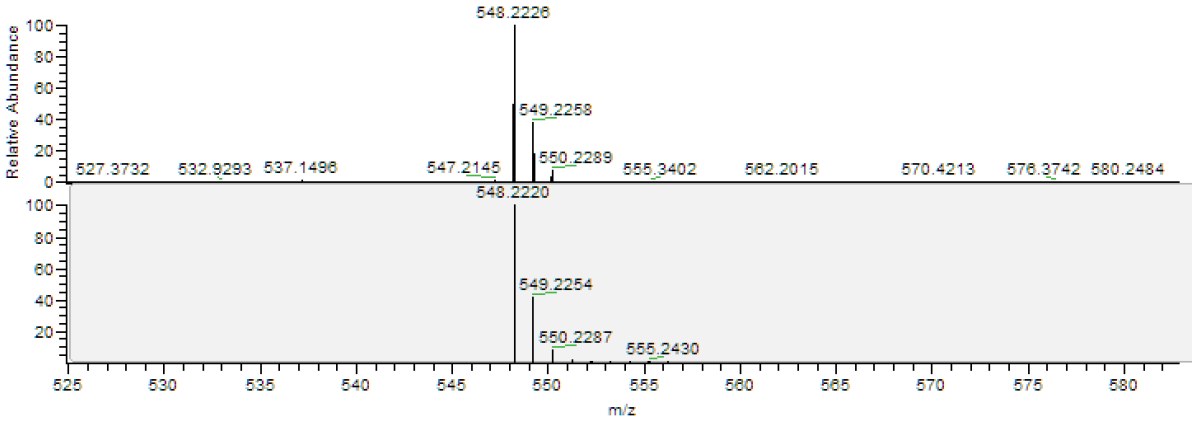

Figure S34. ESI-MS (positive ionisation) spectrum of **OQAO(mes)$_2$** (top) and predicted isotopic profile (bottom).

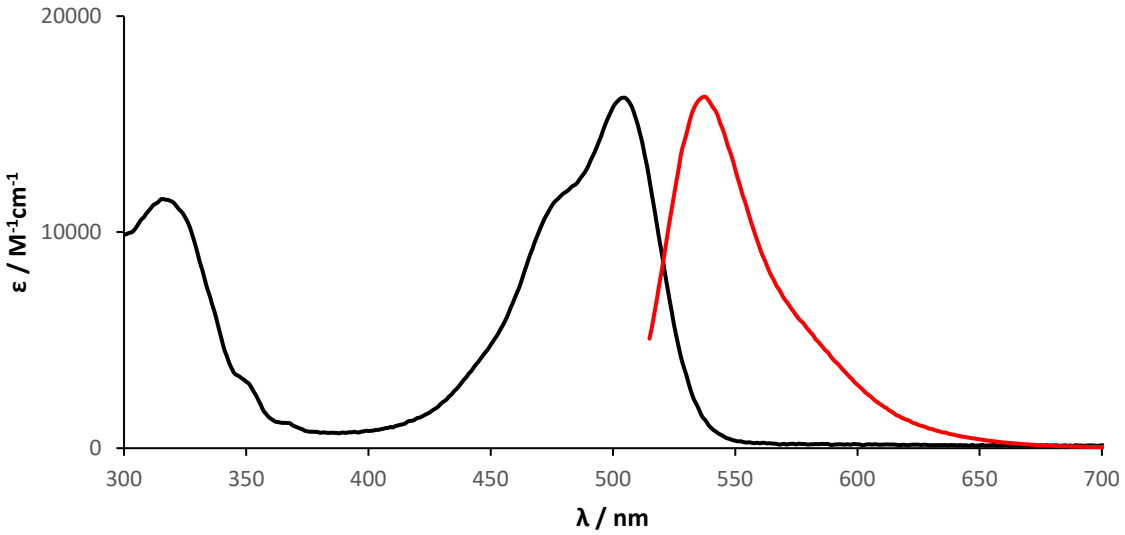

Figure S35. UV-Vis (black) and normalised **fluorescence** (red) of **OQAO(mes)$_2$**.

References

1. E. Eizner, L. A. Martínez-Martínez, J. Yuen-Zhou and S. Kéna-Cohen, *Science Advances*, 2019, **5**, eaax4482.

2. F. C. Courchay, J. C. Sworen, I. Ghiviriga, K. A. Abboud and K. B. Wagener, *Organometallics*, 2006, **25**, 6074–6086.

3. S.-N. Zou, C.-C. Peng, S.-Y. Yang, Y.-K. Qu, Y.-J. Yu, X. Chen, Z.-Q. Jiang and L.-S. Liao, *Org Lett*, 2021, **23**, 958–962.